ChemComm

COMMUNICATION

View Article Online
View Journal

Cite this: DOI: 10.1039/d5cc02188j

Received 19th April 2025,
Accepted 1st July 2025

DOI: 10.1039/d5cc02188j

rsc.li/chemcomm

A direct approach to Zn^{2+} pre-intercalated V_2O_5 cathodes with superior electrochemical performance for aqueous zinc-ion batteries†

Mayank K. Singh,[a] Sarvesh Aware,[a] Pranjal Jaiswal,[a] Sheetal Gupta,[a]
Khushwant Singh,[a] Neha Chaudhary,[a] Govind K. Maurya[a] and Dhirendra K. Rai*[ab]

We report a simple and direct hydrothermal route to synthesize Zn^{2+}-intercalated $V_2O_5{\cdot}nH_2O$ using a zinc metal strip as the Zn^{2+} source—a strategy not previously applied to vanadium oxides. This direct intercalation expands the interlayer spacing and enhances structural stability, delivering significantly improved capacity, rate performance, and cycling stability compared to most of the existing Zn-intercalated V_2O_5 systems obtained by conventional approaches. Density Functional Theory (DFT) calculations reveal reduced band gap and increased electronic states near the Fermi level due to Zn-intercalation, confirming enhanced electronic conductivity. This work offers a novel design pathway toward high-performance cathodes for aqueous Zn-ion batteries.

The growing demand for scalable, safe, and sustainable energy storage has intensified interest in alternatives to lithium-ion batteries. Aqueous zinc-ion batteries (AZIBs) have emerged as promising candidates due to their low cost, use of non-flammable water-based electrolytes, and excellent electrochemical reversibility.[1] Among various cathodes, V_2O_5 stands out for its high capacity and multivalent redox behavior.[2] However, its practical application is hindered by low electronic conductivity ($\sim 10^{-3}$ S cm^{-1}), narrow interlayer spacing ($\sim$4.37 Å), and structural degradation during cycling. These challenges result in poor rate capability and limited cycling life. Overcoming these limitations is essential to advancing AZIB technology and enabling the development of high-performance, durable cathode materials.[3]

Pre-intercalating Zn^{2+} into vanadium oxides overcomes its intrinsic limitations (low conductivity, slow Zn^{2+} diffusion, structural instability) through improved ion kinetics, phase transition stabilization, and enhanced cycling stability. Several groups have reported promising Zn-intercalated V_2O_5 systems. Kundu *et al.* developed $Zn_{0.25}V_2O_5{\cdot}nH_2O$ with $\sim$300 mAh g^{-1} capacity and >80% retention over 1000 cycles.[4] Hu *et al.* reported a Zn^{2+}-pillared vanadium bronze delivering $\sim$450 Wh kg^{-1} and excellent cycling performance.[5] Liu *et al.* showed that ZnV_2O_5 offered enhanced ion transport and structural stability with a capacity of $\sim$300 mAh g^{-1}.[6] However, these methods are often complex, limiting scalability and leading to non-uniform Zn^{2+} distribution—underscoring the need for simpler, scalable approaches.

Herein, we report a novel two-step hydrothermal strategy for synthesizing $Zn_xV_2O_5{\cdot}nH_2O$ *via* $VOPO_4{\cdot}2H_2O$ formation, followed by direct Zn^{2+} intercalation using a zinc metal strip—a method not previously applied to vanadium oxides. This approach enables uniform Zn^{2+} insertion, expands interlayer spacing, and produces a flower-like morphology with high surface area and short diffusion paths. The resulting cathode delivers a high capacity of 324 mAh g^{-1} at 0.1 A g^{-1}, excellent rate performance, and long-term cycling stability. Compared to conventional methods, this simple and scalable route yields superior electrochemical performance, advancing Zn^{2+}-intercalated V_2O_5 as a promising cathode for aqueous zinc-ion batteries.

The synthesis of $Zn_xV_2O_5{\cdot}nH_2O$, as shown in Fig. 1a, was done using a two-step hydrothermal process. In the first step, $VOPO_4{\cdot}2H_2O$ was synthesized by refluxing 4.8 g of V_2O_5 with 26.6 mL of H_3PO_4 in 115 mL of distilled water for 24 h. After refluxing, the mixture was filtered, washed, and dried overnight at 65 °C to get the desired product. In the second step, 100 mg of the resulting $VOPO_4{\cdot}2H_2O$ was dispersed in 10 mL of distilled water with stirring. A polished zinc strip (purity 99.99%) of 1 × 3 cm^2, which had been pretreated with 30% HCl and ethanol to remove surface oxides, was then added to the solution. This mixture was transferred into a 15 mL Teflon-lined stainless-steel autoclave and heated at 120 °C for 3 h. After natural cooling, the product was centrifuged and washed three times with deionized water and ethanol, then dried at 70 °C for 48 h, resulting in a dark green $Zn_xV_2O_5{\cdot}nH_2O$ powder.

---

[a] *Sustainable Energy and Environmental Materials (SEEM) Lab, Department of Metallurgical Engineering and Materials Science, Indian Institute of Technology Indore, Simrol, Indore 453552, India. E-mail: dkrai@iiti.ac.in*

[b] *Microstructure and Texture Engineering Lab, Department of Metallurgical Engineering and Materials Science, Indian Institute of Technology Indore, Simrol, Indore 453552, India*

† Electronic supplementary information (ESI) available. See DOI: https://doi.org/10.1039/d5cc02188j

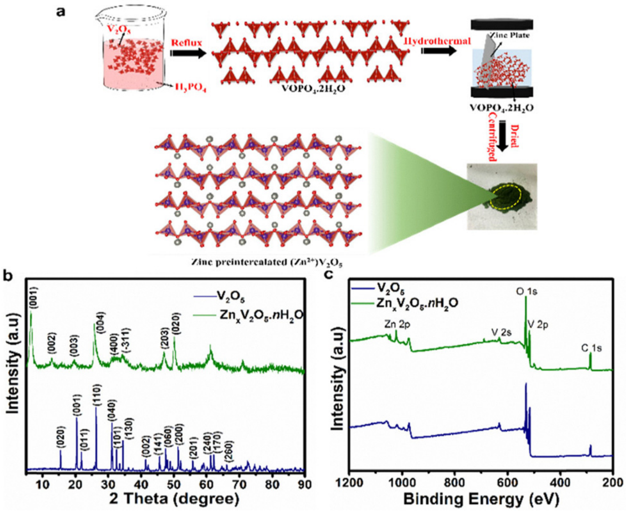

Fig. 1 (a) Synthesis process of $Zn_xV_2O_5{\cdot}nH_2O$, (b) XRD patterns, (c) XPS spectra.

To probe the structural evolution during synthesis, X-ray diffraction (XRD) was performed on all samples. As shown in Fig. 1b, pristine V_2O_5 displays sharp reflections corresponding to an orthorhombic phase (JCPDS No. 41-1426), indicative of high crystallinity.[7] In contrast, the intermediate $VOPO_4{\cdot}2H_2O$ exhibits a tetragonal layered structure (Fig. S1, ESI†), characterized by reflections arising from layers of vertex-sharing $\{PO_4\}$ tetrahedra and $\{VO_6\}$ octahedra.[8–10] Following hydrothermal treatment with a zinc strip, the XRD pattern of $Zn_xV_2O_5{\cdot}nH_2O$ shown in Fig. 1b reverts to the V_2O_5-type framework, accompanied by noticeable shifts in the 00n reflections towards higher 2θ angle, suggesting expanded interlayer spacing due to Zn^{2+} intercalation. Moreover, the formation of a separate ZnO phase was ruled out as PXRD of $Zn_xV_2O_5{\cdot}nH_2O$ does not show any sign of ZnO PXRD pattern (Fig. S2, ESI†). FTIR spectroscopy (Fig. S3, ESI†) was used to identify functional groups and validate Zn^{2+} insertion. Pristine V_2O_5 shows characteristic V═O stretching near 1000 cm^{-1}, asymmetric and symmetric V–O vibrations around 800 and 490 cm^{-1}, respectively. For $Zn_xV_2O_5{\cdot}nH_2O$, additional broad bands at ∼3200 and 1600 cm^{-1} correspond to O–H stretching and bending modes of coordinated water. A distinct absorption near 500 cm^{-1} indicates Zn–O bond formation, confirming Zn^{2+} intercalation into the vanadium oxide matrix.[11,12] XPS analysis (Fig. 1c and Fig. S4a–c, ESI†) further corroborates Zn^{2+} incorporation. The survey spectrum of pristine V_2O_5 shows V 2p, V 2s, and O 1s peaks, while $Zn_xV_2O_5{\cdot}nH_2O$ additionally exhibits Zn $2p_{3/2}$ and $2p_{1/2}$ peaks at 1022.2 and 1036.9 eV, respectively.[13] V $2p_{3/2}$ and $2p_{1/2}$ peaks appear at 517.4 and 525.9 eV, with O 1s peaks at 533.2 and 531.3 eV, assigned to V–O and O–V–O bonds.[14] A C 1s signal, arising from surface-adsorbed adventitious carbon, is also observed in both samples. Morphological analysis by FE-SEM and TEM (Fig. 2a, b, g and h) reveals a lamellar structure for pristine V_2O_5, while $Zn_xV_2O_5{\cdot}nH_2O$ adopts a flower-like architecture composed of radially assembled nanosheets, indicating increased surface area and interlayer spacing. The morphology of intermediate material $VOPO_4{\cdot}2H_2O$ also resembles that of V_2O_5 (Fig. S5, ESI†). EDX spectra (Fig. 2c and e) confirm the presence of V and O in pristine V_2O_5, and uniform Zn incorporation in $Zn_xV_2O_5{\cdot}nH_2O$. Elemental mapping (Fig. 2d and f) further affirms the homogeneous spatial distribution of Zn, V, and O without detectable impurities.

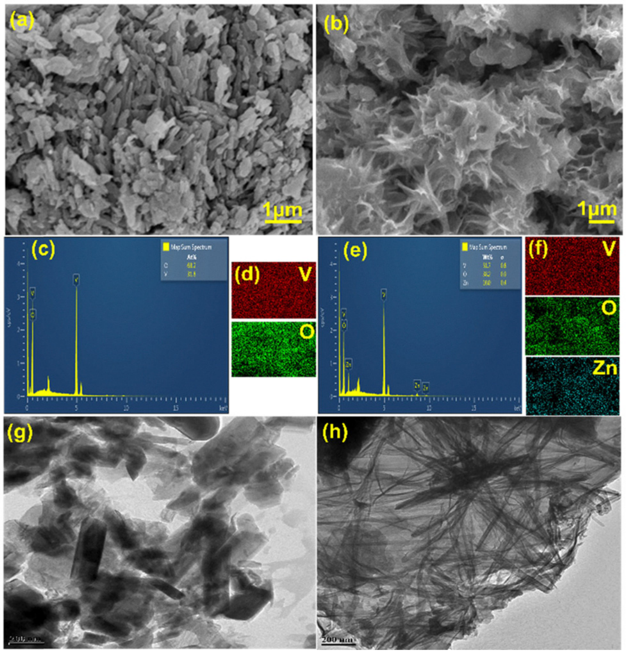

Fig. 2 (a) and (b) FE-SEM images of V_2O_5 and $Zn_xV_2O_5{\cdot}nH_2O$, (c) and (e) EDX of V_2O_5 and $Zn_xV_2O_5{\cdot}nH_2O$. (d) and (f) Elemental mapping of V_2O_5 and $Zn_xV_2O_5{\cdot}nH_2O$, (g) and (h) TEM images of V_2O_5 and $Zn_xV_2O_5{\cdot}nH_2O$.

The electrochemical performance of the materials was evaluated using CR2032-type coin cells assembled with a cathode composed of the active material, a zinc foil anode, a separator, and 3 M $Zn(CF_3SO_3)_2$ as the electrolyte. The cell configuration is illustrated in Fig. 3a, which shows the components of a standard coin-type battery. To assess the electrochemical behavior, cyclic voltammetry (CV) was conducted at a scan rate of 1 mV s^{-1} for both pristine V_2O_5 and $Zn_xV_2O_5{\cdot}nH_2O$ electrodes (Fig. 3b). The CV profiles reveal that $Zn_xV_2O_5{\cdot}nH_2O$ exhibits a markedly enhanced current response and more distinct redox peaks compared to pristine V_2O_5, reflecting superior electrochemical activity. Both electrodes display three well-defined redox peaks centered around ∼1.3 V, ∼1.0 V, and ∼0.6 V. These peaks arise from the stepwise and reversible redox transitions involving V^{5+}/V^{4+} and V^{4+}/V^{3+} couples. The first peak (∼1.3 V) corresponds to the initial Zn^{2+} insertion into the V_2O_5 layers, accompanied by partial V^{5+} reduction. The intermediate peak (∼1.0 V) is indicative of a progressive reduction process and may involve a mixed-valence state or structural rearrangement facilitating further Zn^{2+} intercalation. The third peak (∼0.6 V) is attributed to deeper intercalation and full reduction of V^{4+} to V^{3+}. Collectively, these peaks represent the energetically distinct intercalation stages and multi-electron redox process characteristics of the layered V_2O_5 framework.[15] The improved peak sharpness and intensity in $Zn_xV_2O_5{\cdot}nH_2O$ indicate enhanced redox kinetics and reversibility, which can be attributed to the expanded interlayer spacing induced by Zn^{2+} pre-intercalation. This structural modification facilitates ion diffusion and increases the availability of redox-active sites,

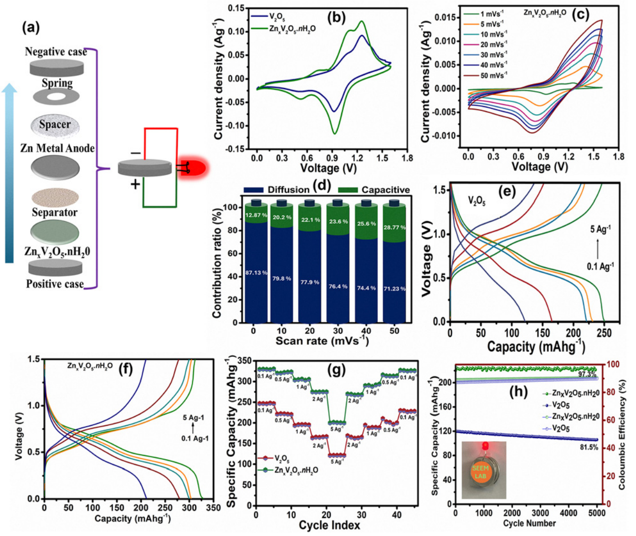

Fig. 3 (a) Schematic representation of cell components, (b) CV comparison of V_2O_5 and $Zn_xV_2O_5{\cdot}nH_2O$ at 1 mV s^{-1}, (c) CV of $Zn_xV_2O_5{\cdot}nH_2O$ at different scan rates, (d) percentage contribution of capacitive and diffusion behavior of $Zn_xV_2O_5{\cdot}nH_2O$, (e) and (f) GCD of V_2O_5 and $Zn_xV_2O_5{\cdot}nH_2O$, (g) rate capability of V_2O_5 and $Zn_xV_2O_5{\cdot}nH_2O$, (h) long term stability and coulombic efficiency of V_2O_5 and $Zn_xV_2O_5{\cdot}nH_2O$ (Inset: demonstration of the device powering red LED).

ultimately leading to superior electrochemical performance. Fig. 3c presents the CV curves of $Zn_xV_2O_5{\cdot}nH_2O$ recorded at various scan rates ranging from 1 to 50 mV s^{-1}. The consistent shape of the curves and the progressive increase in current with scan rate suggest the coexistence of diffusion-controlled and capacitive processes. Although the ΔE_p in CV does not significantly narrow upon Zn intercalation, improved electronic conductivity, reduced charge-transfer resistance, and enhanced capacity collectively confirm reduced polarization and improved kinetics as supported by DFT and EIS results discussed later. The broad, symmetric redox peaks further indicate substantial pseudocapacitive contributions to charge storage, characteristic of fast and reversible surface or near-surface redox reactions.

To distinguish and quantify the contributions of capacitive and diffusion-controlled processes, Dunn's method was applied (Fig. 3d and Fig. S6, ESI†).[16] The analysis reveals that the faradaic (diffusion-controlled) contribution decreases from 87% at 1 mV s^{-1} to 71% at 50 mV s^{-1}. This declining trend is attributed to kinetic constraints at higher scan rates: as the scan rate increases, the time available for ion diffusion and bulk redox transformations within the electrode becomes limited. As a result, slower faradaic reactions, which involve ion insertion and structural reconfiguration, become increasingly suppressed. Conversely, faster surface-limited capacitive processes dominate under such conditions, as they are less reliant on ion transport through the bulk material. Fig. 3e and f display the galvanostatic charge–discharge (GCD) profiles of pristine V_2O_5 and $Zn_xV_2O_5{\cdot}nH_2O$, respectively, recorded at current densities ranging from 0.1 to 5 A g^{-1}. Pristine V_2O_5 delivers a specific capacity of 250 mAh g^{-1} at 0.1 A g^{-1}, which declines sharply to 124 mAh g^{-1} at 5 A g^{-1} (~50% retention). In contrast, $Zn_xV_2O_5{\cdot}nH_2O$ achieves a higher capacity of 324 mAh g^{-1} at 0.1 A g^{-1} and retains 210 mAh g^{-1} at 5 A g^{-1} (~65% retention), along with visibly reduced voltage polarization. This improved performance reflects enhanced Zn^{2+} intercalation kinetics and superior ion transport enabled by the expanded interlayer spacing and increased redox-active sites introduced through Zn^{2+} pre-intercalation. The rate performance comparison shown in Fig. 3g also highlights this contrast: while V_2O_5 undergoes a steep capacity drop at elevated current densities, $Zn_xV_2O_5{\cdot}nH_2O$ maintains excellent capacity retention, underscoring its robust structural stability and superior electrochemical reversibility under high-rate conditions.

In AZIB, it is known that Zn^{2+} intercalation occurs alongside H^+ co-intercalation for charge storage. To better understand this process, we monitored pH changes during repeated cycling and measured charge storage capacity using a Nafion separator (see Fig. S7, ESI†). The results indicated a very low contribution to charge storage from H^+ intercalation. The quality of the zinc strips plays a critical role in determining the uniformity of Zn^{2+} intercalation and overall electrochemical performance. Surface oxides, such as ZnO, and metallic impurities can disrupt dissolution kinetics and affect vanadium redox states. Our controlled experiment that utilized a commercially available zinc alloy strip (PR Metal Alloy) instead of high-purity zinc foil showed a 25% reduction in capacity (280 mAh g^{-1}) (Fig. S8, ESI†). This finding underscores the importance of using pure zinc sources for optimal performance.

To understand the ion transportability and conductive nature, EIS study was performed (Fig. S9, ESI†), revealing that $Zn_xV_2O_5{\cdot}nH_2O$ exhibits markedly lower equivalent series resistance R_s (1.2 Ω) and charge transfer resistance R_{ct} (32.3 Ω) compared to pristine V_2O_5 (R_s = 2.9 Ω, R_{ct} = 44.56 Ω), indicative of improved ionic transport and interfacial charge transfer kinetics. Furthermore, the long-term cycling performance of both materials was also assessed at a current density of 5 A g^{-1} (Fig. 3h). The $Zn_xV_2O_5{\cdot}nH_2O$ electrode retains 97.3% of its initial capacity after 5000 cycles, whereas pristine V_2O_5 shows only 81.5% retention over the same number of cycles. This comparison clearly demonstrates the superior cycling stability of the Zn-intercalated electrode, which can be attributed to its enhanced structural robustness and resistance to degradation during repeated charge–discharge cycles. Also, $Zn_xV_2O_5{\cdot}nH_2O$ demonstrates an excellent energy density of 231 Wh kg^{-1}, at 0.1 A g^{-1}, compared to 185 Wh kg^{-1} for pristine V_2O_5. To assess post-cycling morphological and compositional stability of $Zn_xV_2O_5{\cdot}nH_2O$, FESEM, EDX, and elemental mapping analyses were conducted (Fig. S10a–d, ESI†), suggesting no significant morphological alteration and a uniform presence of V, Zn, and O, along with minor residual elements (C, F, and S) originating from the electrolyte. The homogeneous elemental distribution observed in elemental mapping indicates that the structural and chemical integrity of $Zn_xV_2O_5{\cdot}nH_2O$ is well-preserved after prolonged cycling. Additionally, to demonstrate practical applicability, two identical coin cells connected in series were successfully used to power red light-emitting diodes (LEDs), as shown in the inset of Fig. 3h. A comparative performance table (Table. S1, ESI†) highlights that the $Zn_xV_2O_5{\cdot}nH_2O$ synthesized *via* present method exhibits excellent charge storage capacity, rate capability, and superior cycling stability compared to conventional synthesis routes reported previously, except entry 3. However, rate capability in entry 3 is still lower than the present material.

To investigate the Zn^{2+} storage mechanism, ex-situ XRD was performed on $Zn_xV_2O_5{\cdot}nH_2O$ at charged and discharged states (Fig. S11, ESI†). Reversible shifts in the (00n) peaks indicate

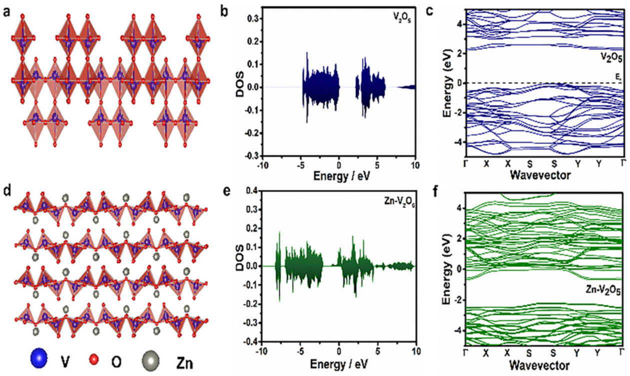

Fig. 4 (a) and (d) Optimized structure of V_2O_5 and $Zn_xV_2O_5{\cdot}nH_2O$, (b) and (e) DOS of V_2O_5 and $Zn_xV_2O_5{\cdot}nH_2O$ (c) and (f) Band Gap of V_2O_5 and $Zn_xV_2O_5{\cdot}nH_2O$.

interlayer spacing changes linked to Zn^{2+} insertion/extraction. A lower-angle shift during discharge confirms layer expansion, while the reverse shift upon charging reflects contraction. Further, to rationalize the superior electrochemical performance of Zn^{2+}-intercalated V_2O_5 compared to pristine V_2O_5, first-principles density functional theory (DFT) calculations were performed to investigate the effect of Zn^{2+} intercalation on the electronic structure and density of states (DOS), offering insights into the observed enhancement in conductivity. The details of the computational study are provided in the ESI.† The optimized structural models of pristine and Zn-intercalated V_2O_5 are shown in Fig. 4a and d, respectively. Pristine V_2O_5 adopts a layered orthorhombic structure composed of edge- and corner-sharing VO_5 square pyramids, with layers stacked along the *c*-axis and held together by weak van der Waals forces. Upon Zn^{2+} intercalation, Zn atoms (depicted as grey spheres) are inserted into the interlayer space, leading to an expansion in interlayer distance. This structural modification facilitates Zn^{2+} diffusion by creating more accessible channels, thereby enhancing electrochemical performance. To gain deeper insight into the electronic effects of intercalation, the total density of states (DOS) and band structures of both materials were analyzed (Fig. 4b–f). Compared to pristine V_2O_5, the Zn-intercalated material exhibits a notable increase in the density of states (DOS) near the Fermi level. This enhancement is primarily attributed to the incorporation of Zn 3d orbitals into the valence band, in addition to the existing contributions from V-3d and O-2p orbitals, as evident from the partial density of states (PDOS) analysis near the Fermi level (Fig. S12, ESI†). The increased DOS arises from electronic interactions between the intercalated Zn^{2+} ions and the V_2O_5 framework, leading to partial charge transfer and improved orbital hybridization, which collectively enhance the material's electronic conductivity. The elevated DOS near the Fermi level suggests enhanced electronic conductivity. Band gap calculations further support this observation, revealing a reduction from 2.1 eV in pristine V_2O_5 to 1.8 eV in Zn-intercalated V_2O_5, indicating a narrowing of the band gap and improved charge transport characteristics.

These computational results clearly demonstrate that Zn^{2+} intercalation not only expands the crystal lattice but also modifies the electronic structure of V_2O_5, collectively contributing to enhanced ionic and electronic conductivity. This dual structural and electronic modulation aligns well with the experimental observations and emphasizes the promise of Zn-intercalated V_2O_5 as a high-performance cathode material for aqueous Zn-ion batteries.

In conclusion, the Zn^{2+}-intercalated $V_2O_5{\cdot}nH_2O$ cathode developed *via* a straightforward two-step hydrothermal method, employing a direct Zn metal strip as the Zn^{2+} source, exhibits significantly enhanced electrochemical performance compared to pristine V_2O_5. This direct intercalation approach enables uniform Zn^{2+} insertion into the vanadium oxide layers, leading to expanded interlayer spacing, improved ion diffusion, and enhanced redox kinetics. As a result, the resulting $Zn_xV_2O_5{\cdot}nH_2O$ delivers high specific capacity, excellent rate performance, and outstanding cycling stability. Notably, it outperforms most of the previously reported Zn-intercalated $V_2O_5{\cdot}nH_2O$ materials synthesized by conventional methods, demonstrating the effectiveness of this simple yet efficient strategy for optimizing electrochemical behavior. These findings highlight the promise of Zn-intercalated vanadium oxides as advanced cathode materials for next-generation aqueous zinc-ion batteries targeting sustainable energy storage.

Conflicts of interest

There are no conflicts of interest to declare.

Data availability

The authors confirm that the data supporting the findings of this study are available within the article and its ESI.†

Notes and references

1 G. Li, L. Sun, S. Zhang, C. Zhang, H. Jin, K. Davey, G. Liang, S. Liu, J. Mao and Z. Guo, *Adv. Funct. Mater.*, 2024, **34**, 2301291.
2 A. Guo, Z. Wang, L. Chen, W. Liu, K. Zhang, L. Cao, B. Liang and D. Luo, *ACS Nano*, 2024, **18**, 27261–27286.
3 K. Zhu and W. Yang, *Acc. Chem. Res.*, 2024, **57**, 2887–2900.
4 D. Kundu, B. D. Adams, V. Duffort, S. H. Vajargah and L. F. Nazar, *Nat. Energy*, 2016, **1**, 16119.
5 P. Hu, M. Yan, T. Zhu, X. Wang, X. Wei, J. Li, L. Zhou, Z. Li, L. Chen and L. Mai, *ACS Appl. Mater. Interfaces*, 2017, **9**, 42717–42722.
6 Y. Liu, Y. Liu and X. Wu, *Batteries Supercaps*, 2023, **6**, e202200461.
7 I. Kosta, Ch Navone, A. Bianchin, E. García-Lecina, H. Grande, H. I. Mouko, J. Azpeitia and I. García, *J. Alloys Compd.*, 2021, **856**, 158069.
8 J. A. Z. Martínez, S. E. G. Náñez, E. Le Calvez, R. Lucio Porto, I. E. M. Cortez, T. Brousse and L. A. L. Pavón, *J. Electrochem. Soc.*, 2021, **168**, 070531.
9 Y. Liu, X. Xiao, X. Liu, L. L. Cui and Y. Gong, *J. Mater. Chem. A*, 2022, **10**, 912–927.
10 J. Wang, S. Tan, F. Xiong, R. Yu, P. Wu, L. Cui and Q. An, *Chem. Commun.*, 2020, **56**, 3805–3808.
11 C. Xiong, A. E. Aliev, B. Gnade and K. J. Balkus, *ACS Nano*, 2008, **2**, 293–301.
12 D. Jugović, M. D. Milović, T. Barudžija, M. Kuzmanović, M. Vujković and M. Mitrić, *Materials*, 2022, **15**, 9041.
13 T. K. Le, M. Kang, S. W. Han and S. W. Kim, *RSC Adv.*, 2018, **8**, 41317–41322.
14 J. Zhou, L. Shan, Z. Wu, X. Guo, G. Fang and S. Liang, *Chem. Commun.*, 2018, **54**, 4457–4460.
15 Y. Li, Z. Huang, P. K. Kalambate, Y. Zhong, Z. Huang, M. Xie, Y. Shen and Y. Huang, *Nano Energy*, 2019, **60**, 752–759.
16 Z. Wu, C. Lu, Y. Wang, L. Zhang, L. Jiang, W. Tian, C. Cai, Q. Gu, Z. Sun and L. Hu, *Small*, 2020, **16**, 2000698.